VTT Technical Research Centre of Finland

Comprehensive characterization of irradiation induced defects in ceria: Impact of point defects on vibrational and optical properties

Chauhan, Vinay; Ferrigno, Joshua; Adnan, Saqeed; Pakarinen, Janne; He, Lingfeng; Hurley, David; Khafizov, Marat

Published in:
Journal of Applied Physics

DOI:
10.1063/5.0099189

Published: 25/08/2022

Document Version
Peer reviewed version

Journal of Applied Physics

AIP Publishing

Comprehensive characterization of irradiation induced defects in ceria: Impact of point defects on vibrational and optical properties

Vinay S. Chauhan[1], Joshua Ferrigno[1], Saqeeb Adnan[1], Janne Pakarinen[2], Lingfeng He[3], David H. Hurley[3], and Marat Khafizov[1*]
[1] Department of Mechanical and Aerospace Engineering, The Ohio State University, Columbus, OH, 43210 USA
[2] VTT Technical Research Centre of Finland Ltd, Espoo, FI-02044 VTT, Finland
[3] Idaho National Laboratory, Idaho Falls, ID 84315, USA
* Corresponding author khafizov.1@osu.edu

Abstract

Validation of multiscale microstructure evolution models can be improved when standard microstructure characterization tools are coupled with methods sensitive to individual point defects. We demonstrate how electronic and vibrational properties of defects revealed by optical absorption and Raman spectroscopies can be used to compliment transmission electron microscopy (TEM) and X-ray diffraction (XRD) in characterization of microstructure evolution in ceria under non-equilibrium conditions. Experimental manifestation of nonequilibrium conditions was realized by exposing cerium dioxide (CeO_2) to energetic protons at elevated temperature. Two sintered polycrystalline CeO_2 samples were bombarded with protons accelerated to a few MeVs. These irradiation conditions produced a microstructure with resolvable extended defects and a significant concentration of point defects. A rate theory (RT) model was parametrized using the results of TEM, XRD and thermal conductivity measurements to infer point defect concentrations. An abundance of cerium sublattice defects suggested by the RT model is supported by Raman spectroscopy measurements, which shows peak shift and broadening of the intrinsic T_{2g} peak and emergence of new defect peaks. Additionally, spectroscopic ellipsometry measurements performed in lieu of optical absorption revealed the presence of Ce^{3+} ions associated with oxygen vacancies. This work lays the foundation for a coupled approach that considers a multimodal characterization of microstructures to guide and validate complex defect evolution models.

Keywords: cerium dioxide, defect characterization, microstructure evolution, radiation damage.

1. Introduction

Physical and chemical behavior of metal oxides is important for an array of energy applications, including solid oxide fuel cells (SOFC), catalysis, electrical storage, and nuclear energy applications (*1-5*). For many of these applications, oxygen vacancies and cation substitutional impurities play an important role in determining their behavior, and therefore have been extensively studied in doped ceria and zirconia (*6-8*). However, cations' thermal diffusion is also significant for grain growth and sintering of polycrystalline ceramics (*9, 10*). Cation defects in isolation have been studied to a lesser extent, due to their higher formation energies and low concentration under thermal equilibrium (*11, 12*). Therefore, the individual impact of cation related defects is negligible for most applications, except where the ionic compounds are exposed to irradiation by energetic particles (*13-15*). The bombardment with energetic particles displaces both cations and anions from their equilibrium positions (*16*). Under these conditions, the mobility of generated self-interstitials and vacancies, their mutual recombination, and clustering into extended defects determine the radiation stability of materials (*5, 15*). Thus, an improved understanding of materials irradiation response is intimately coupled to the availability of experimental methods able to characterize cation vacancies and self-interstitials.

Commonly used methods to investigating microstructure evolution under irradiation include X-ray diffraction (XRD) analysis (*14, 17, 18*), Rutherford back-scattering (RBS) spectroscopy (*19, 20*), optical spectroscopy (*21-23*), and transmission electron microscopy (TEM) (*24-27*). Further analysis, focusing on point defects and small clusters, has been done to complement those methods, including positron annihilation spectroscopy (*28-30*), X-ray synchrotron techniques (*31, 32*), and Raman spectroscopy (*33, 34*). Recent applications of non-destructive methods for measuring thermal transport and elastic properties have emerged as attractive tools for characterization of

microstructure evolution (*35-39*). Our aim is to capture microstructural processes across multiple scales in a single study instead of characterizing each defect in isolation.

In general, the extent of multiscale processes under long-term irradiation is very broad, including creation of dislocation networks and void formation (*5, 40, 41*). Our focus here is on the early stage of defect evolution with an emphasis on atomic level point defects, which includes their atomic arrangement, electronic structure, and processes involving their migration, mutual recombination, and clustering into extended defects. This work builds upon previous characterization of the same sample set using TEM, XRD and thermal conductivity measurement (*42*). TEM was used to characterize dislocation loops, while XRD and thermal conductivity measurements were used to measure the integrated influence of all defects. In this report, we expand the characterization to include Raman spectroscopy and optical ellipsometry (OE) to characterize individual point defects. Because characterization of cation defects using the aforementioned optical spectroscopies has not been considered in detail previously, we first apply rate theory (RT) modeling to understand the extent of cation defect formation and clustering. This model accounts for monomer generation, recombination, and dislocation loop evolution without relying on more comprehensive cluster dynamics modeling (*16, 43*). Dislocation loop density, lattice constant changes, and mesoscale thermal conductivity measurements were used to parametrize our rate theory model for defect evolution.

The schematic shown in Fig. 1 depicts the early stage of defect evolution in cerium dioxide (CeO_2) under irradiation represented by such rate theory modeling (*42*). Microstructure evolution is described by an initial linear increase in monomer concentration proportional to the generation rate, followed by a quasi-equilibrium state where vacancies and interstitials mutually recombine, and clustering of interstitials into dislocation loops. While this description doesn't recognize

different charge states of ions and presence of defect clusters (*44-46*), it provides a simple picture that captures independent evolution of cation and anion defects of ions. Fig. 1 also illustrates characteristic features of measurement tools used to characterize point defects. The overall goal of this effort is to use this understanding to aid in the interpretation of our optical spectroscopy results.

We demonstrate the potential of Raman spectroscopy and optical ellipsometry to characterize point defects across both cation and anion sublattices. Accordingly, this work addresses the disparity between experimental analysis of cation interstitials and vacancy as compared to oxygen sublattice and cation substitutional defects in ceramic oxides.

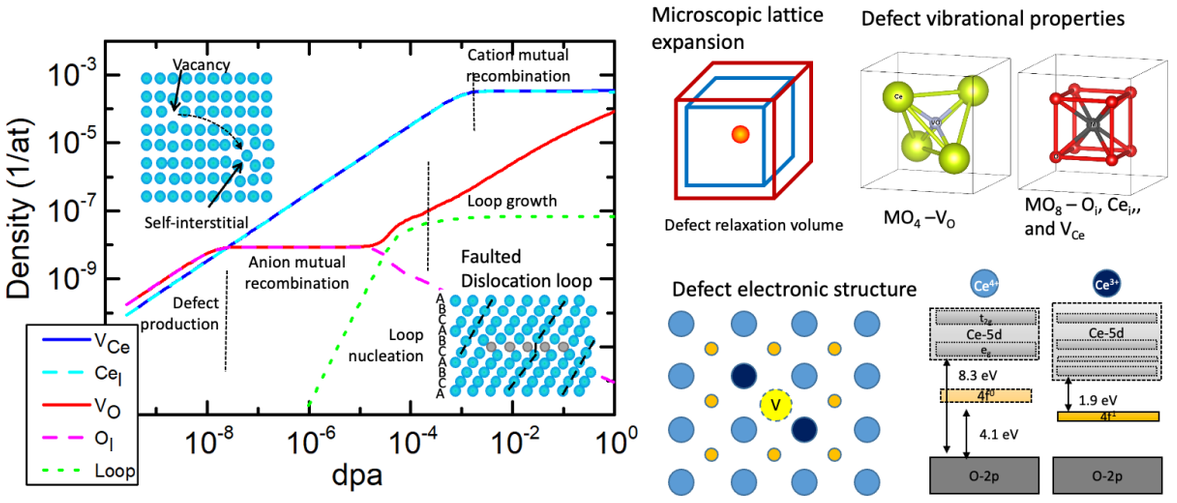

Figure 1. Early stages of defect evolution in CeO_2. Left: Results from a rate theory model showing different stages of microstructure evolution. Right: Characteristic features of point defects making them observable using various experimental tools. XRD is used to measure lattice expansion, the vibration modes of defects are measured using Raman spectroscopy, and electronic structure of the defects is revealed using optical absorption measurements.

2. Experimental Methods

Sample preparation by exposure to energetic ions has been previously reported in (*42*). The polycrystalline sintered ceria pellet samples were purchased from Alfa Aesar. Central regions of two disk-shaped samples were exposed to protons at two different ion currents of 5 µA (LF) and 15 µA (HF), and corresponding flux rates of 1.4×10^{13} and 4.2×10^{13} H^+/cm^2s to the same total fluence. This configuration allowed us to obtain regions of the samples exposed to environmental condition of the chamber but not irradiated. The ion energies applied to both flux rates were 1.5, 2.0, and 2.5 MeV. The fluences were set as 5×10^{17}, 7.5×10^{17} and 1×10^{18} ion/cm^2 for ion energies of 1.5, 2.0, and 2.5 MeV, respectively. The conditions of multi energy irradiation were designed to reduce the amount of implanted hydrogen ions at the peak implantation depth, and thus prevent sample blistering. A third undamaged reference (R) sample was used to compare the effects of irradiation. The ion flux was chosen as the variable irradiation parameter, as it provides a broader defect spectrum as compared to purely dose dependent parametrization. The relevant parameters of all samples are summarized in Table I.

Table I. Irradiation conditions for CeO_2 samples.

Sample ID	**Ion flux (10^{13} H^+/cm^2s)**	**Dose rate (10^{-6} dpa/s)**	**Plateau damage (dpa)**	**Temperature (°C)**
LF	1.4	0.87	0.14	600 ± 50
HF	4.2	2.6	0.14	600 ± 50

SRIM-2013 code was used to estimate damage profile in units of displacements per atom (dpa) in a full cascade simulation mode (*47*). The threshold displacement energies of 44 and 33 eV were used for Ce and O, respectively, and the density of CeO_2 was taken as 7.21 g/cm^3. The calculated displacement damage and implanted hydrogenprofiles are shown in Fig. S1 of the Supplementary Information Document (SI) and the amount of damage in the plateau region is listed in Table I

(*42*). Since the vacancy concentration is significantly larger than implanted H^+ ion concentration in the plateau damage region, the impact of implanted ions was neglected in the subsequent analysis.

Raman spectra were collected using a Renishaw® inVia confocal Raman Microscope in backscattering geometry using a 457 nm wavelength laser, corresponding to 2.71 eV, below the band gap of ceria (3.4 eV). The spectra were collected over a 250-1500 cm^{-1} window that captures known CeO_2 Raman peaks. A 50× high magnification objective was used to achieve few μm spatial resolution and ensure a small Rayleigh depth limiting signal collection to the damaged portion of the sample. In the case of irradiated samples, the spectra were collected from two different regions, one from the area exposed to the ion beam and another from a region not impacted by the ion beam. This was done to isolate the effects of exposing the samples to the high temperature vacuum environment of the irradiation chamber. The peaks observed in the spectra were fitted using a Gaussian function to determine peak intensity, position, and width.

Optical dielectric constant characterization of the samples was performed using an alpha-SE ellipsometer (J.A. Woollam Co., Inc.) in the wavelength range from 370 - 850 nm (1.45 - 3.35 eV), with an angle of incidence of 70° for the reference sample, and 65° for the LF and HF samples. The optical permittivity of the damaged region was extracted using CompleteEASE® software (J.A. Woollam Co., Inc.) based on known optical properties of bulk ceria (*48-50*). The size of the OE beam was on the order of 1 mm and larger than the unirradiated rim region, not allowing us to probe this part of the sample.

3. Results

Characterization of extended defects using TEM, lattice constant change measurement using XRD, and thermal conductivity measurement of these samples were previously reported in (*42*) and summarized in Table II. These results were used to parametrize the RT model for dislocation loop evolution, whose output can also be used to quantify point defects (*15, 23*). Raman spectroscopy and optical ellipsometry were performed to characterize the point defects in order to provide further validation for the rate model. Visual appearance of the irradiated samples allowed us to isolate the regions that were exposed to the ion beam.

Table II. Summary of TEM, XRD and MTR results (*42*)

Sample ID	**Dislocation loops (TEM)**		**XRD**	**MTR**
	diameter (nm)	density (10^{22} m^{-3})	Swelling (10^4 $\Delta a/a_0$)	Thermal conductivity (W/m·K)
R	-	-	-	14.1±0.2
LF	3.58 ± 0.99	0.65	7 ± 5	11.8±0.1
HF	4.00 ± 1.01	1.18	32 ± 5	10.7±0.1

3.1 Raman Spectroscopy

Representative Raman spectra are shown in Fig. 2. All spectra exhibit a peak at 464.8 cm^{-1}, which is characteristic of fluorite structures and corresponds to a phonon mode with F_{2g} symmetry (*20*). In addition, a broad feature was observed at 580 cm^{-1} in the irradiated samples (Fig. 2), which we refer to as the defect (D) peak for the remainder of the article. This peak was not resolvable in the regions of the irradiated samples that were not exposed to protons. Finally, a third peak at 1194.5 cm^{-1} was only detected in the unirradiated sample. This peak has been assigned to the second order longitudinal optical (2LO) phonon, which is the overtone of the first order LO.

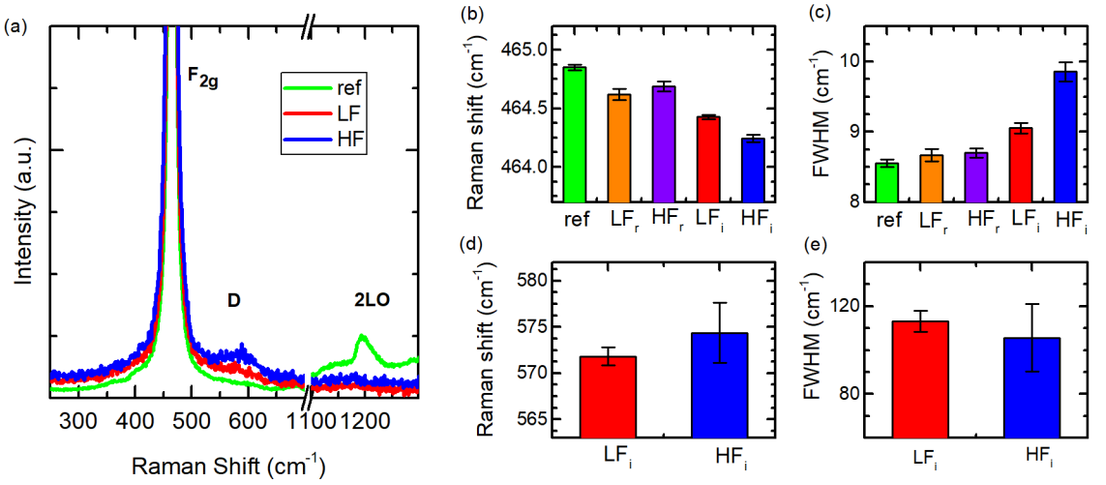

Figure 2. (a) Raman spectra of the ceria samples. Fitting parameter of the experimental spectra using Gaussian function (b) location of F_{2g} peak (c) FWHM of F_{2g} peak (d) position of D peak (e) FWHM of D peak. Subscripts *i* refers to irradiated section of the sample and *r* refers to part of the samples only exposed to high temperature environment of the irradiation chamber.

Careful examination of the spectra reveals that the intensity and width of F_{2g} peak depends on the sample treatment. To investigate this further, we performed a detailed analysis of the peak position, intensity, and FWHM of the F_{2g} and D peaks using Gaussian peak fitting. The graphs shown in Figs. 2 (b) and (c) display the trends related to the F_{2g} peak. The peak position and FWHM of the unirradiated region of the samples are comparable to that of the R sample, indicating that the vacuum inside the irradiation chamber has notably lower impact on the observed changes, and irradiation damage is the dominant mechanism for microstructure evolution. Additionally, the redshift and broadening of F_{2g} peak in irradiated samples are in agreement with the previous reports on irradiated or doped CeO_2 (*20, 51*). Peak shift is larger in the HF than in the LF sample, consistent with lattice expansion previously revealed using XRD (Table II).

Table III. Summary of Raman spectra analysis.

Sample ID	Raman Shift (cm^{-1})	FWHM (cm^{-1})	Intensity ratio (I_D/I_{F2g})	
			Oxygen vacancy, D_1	MO_8 complex, D_2
R	464.85 ± 0.02	8.55 ± 0.05	-	
LF_r	464.62 ± 0.05	8.66 ± 0.09	-	
HF_r	464.69 ± 0.04	8.70 ± 0.07	-	
LF_i	464.43 ± 0.02	9.05 ± 0.07	0.038±0.002	0.050±0.005
HF_i	464.24 ± 0.03	9.86 ± 0.13	0.019±0.001	0.082±0.004

The 2LO peak is only present in the R sample and is absent in irradiated samples. It is termed as a fingerprint for the quasi-perfect fluorite structure (*52, 53*). Activation of this 2LO mode can be attributed to the multiphonon relaxation by the resonance Raman effect (*54*). The disappearance of the 2LO peak in the LF and HF is likely owed to the accumulation of radiation-induced defects, as it has been previously reported that the presence of dopants or non-stoichiometry in the structure leads to a decrease in the intensity of the 2LO peak (*55*).

The D peak appears only in the presence of defects and in general has been attributed to the breakdown of Raman selection rules (*56*). Many studies have assigned the D band to the LO mode with F_{1u} symmetry, which is an infrared active and Raman-forbidden mode in the ideal fluorite structure. However, localized vibration modes of defect complexes are able to satisfy necessary symmetry requirements for Raman activity (*57, 58*).

3.2 Optical Ellipsometry

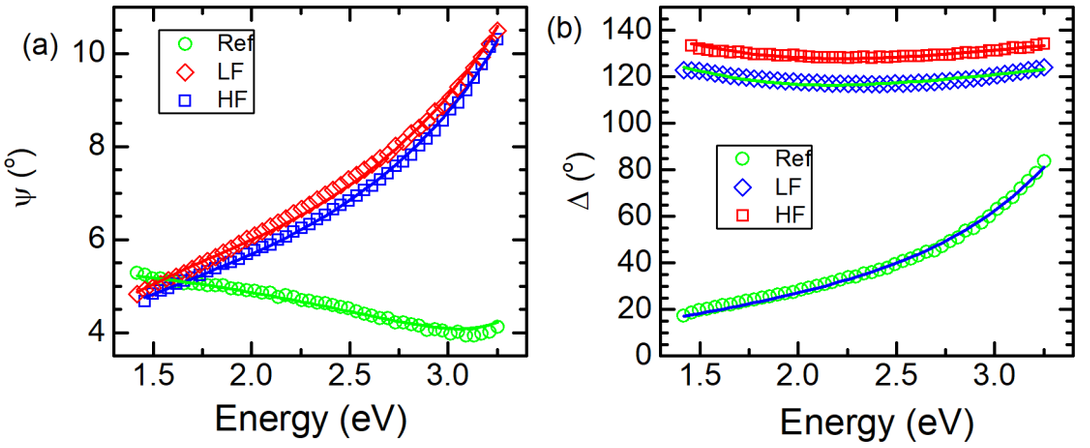

Figure 3. Raw and model data from optical ellipsometry measurements. Data points represent experimental (a) ψ and, (b) Δ values, while the solid lines represent the model lines after fitting as explained in the main text.

Optical ellipsometry measures the amplitude ratio ψ and phase difference Δ between incident and reflected light for s- and p-polarizations, from which the complex dielectric function $\tilde{\varepsilon}(\omega) = \varepsilon_1(\omega) + i\varepsilon_2(\omega)$ is determined (*59*). The raw data shown in Fig. 3 was analyzed by considering a number of electronic transitions each described by Lorentz oscillators identified by peak position (E_o), width (B_o), and oscillator strength (A_o) using (*23, 50, 59*):

$$\varepsilon = \varepsilon_1 + i\varepsilon_2 = \varepsilon_\infty + \frac{A_o B_o E_o}{E_o^2 - E^2 - iEB_o} \quad (1)$$

All samples were assumed to be homogeneous across the probing depth. This is justified when one considers relatively uniform damage profile across top 10 μm (Fig. S1) and a smaller optical penetration depth δ_p estimated to be less than 1 μm across the investigated spectrum (1.45 to 3.35 eV). Analysis of ellipsometry results also considered surface roughness as a fitting parameter.

Data fitting for the pristine sample R was done considering only two oscillators, each corresponding to intrinsic electronic transitions of perfect ceria (*49*). Prior to fitting the ellipsometry data, previously published data from Patsalas et. al. was used to identify the location and the widths of the intrinsic transitions of unirradiated ceria (*50*). The positions of the intrinsic oscillators were found to be E_o ~4.1 eV and ~8.3 eV. The lower energy oscillator corresponds to the O2p→Ce4f electronic transition, while the higher energy oscillator corresponds to the O2p→Ce5d transition (*49*). Once both the width and centroid of the peaks were obtained from the literature, CompleteEase was used to fit the oscillator strength of the intrinsic bands together with ε_∞.

Table IV. Fitting of the spectroscopic ellipsometry results using Lorentz oscillators model (Eq. 1).

Sample ID	R	LF	HF
ϵ_∞	1.05±0.01	1.10±0.05	1.1±0.05
A_{o1}	7.96±0.06	9.7±0.2	8.7±0.2
B_{o1} (eV)	0.45*	0.45*	0.45*
E_{o1} (eV) 2p→4f	4.07*	4.07*	4.07*
A_{o2}	4.5±0.1	3.8±0.1	4.2±0.2
B_{o2} (eV)	6.33*	6.33*	6.33*
E_{o2} (eV) 2p→5d	8.35*	8.35*	8.35*
A_{o3} (a.u.)	-	0.27±0.01	0.24±0.01
B_{o3} (eV)	-	2.0±0.2	2.0±0.2
E_{o3} (eV) defect	-	1.9±0.1	1.9±0.1

* - Fixed parameters obtained from Patsalas et. al.(*50*)

The irradiated samples were fitted using three Lorentz oscillators, where the positions (E_o) and width (B_o) of the intrinsic oscillators were fixed based on the parameters for sample R, while A_o of the intrinsic oscillators and all parameters of the 3rd oscillator were used as fitting parameters. This analysis replicates the procedure previously outlined in (*23*).

The model values of ε_1 and ε_2 are plotted in Fig. 4, (corresponding values for n and k are available in Fig. S2 of SI) and Lorentz peak parameters are listed in Table IV.

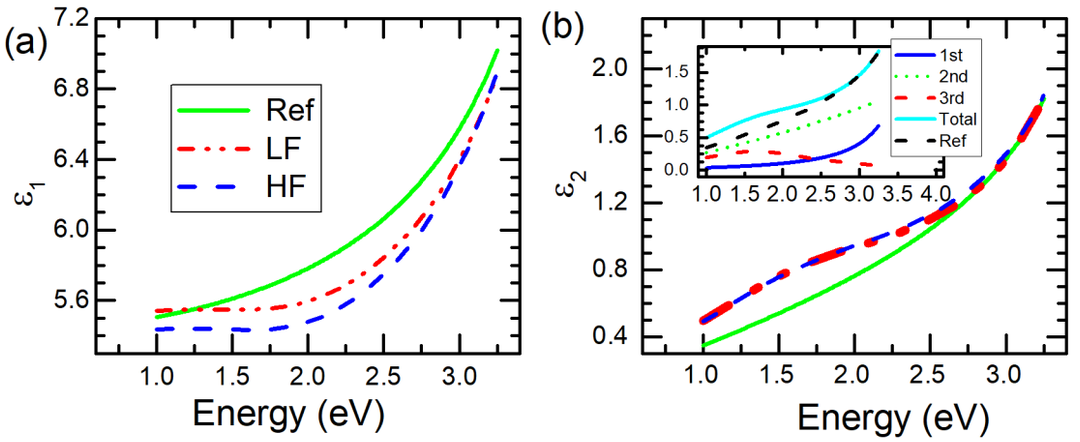

Figure 4. The calculated values of dielectric constants from the model as described in the main text. (a) The real part of the dielectric constant, ϵ_1 and (b) the imaginary part of dielectric constant, ϵ_2, and individual contribution of model dielectric constants by oscillator for low flux sample.

The strength of the oscillator is proportional to the number of available electronic states from which electrons originate and transition to (*60*). It can be observed that the intensities of intrinsic peaks undergo slight changes (Table IV). While 2p-4f oscillator strength increases, the intensity of 2p-5d transition becomes weaker. Unfortunately, the sensitivity analysis suggests that these values do not represent the unique solution, primarily due to the fact that these transition energies lay outside of the experimental window and any observed trends have a large uncertainty to be able to attribute those to a particular physical process. Nevertheless, the defect peak is located

within the experimental window and has a higher certainty. We observe that the defect peak is stronger in the LF sample.

4. Discussion

To put the above optical spectroscopy results in perspective, we need to consider microstructure evolution under irradiation in detail. The TEM results provide a direct, quantifiable information on the characteristics of the extended defects, however the interpretation of spectroscopy results is not trivial. While we postulate that lattice expansion and the emergence of additional peaks in Raman and dielectric optical spectra are indicators for point defects, assignment of these features to a particular defect type requires further analysis.

We assume that the primary defects generated upon irradiation of CeO_2 with protons are interstitials and vacancies on both sublattices, namely oxygen interstitial (O_I), oxygen vacancy (V_O), cerium interstitial (Ce_I), and cerium vacancy (V_{Ce}) (*61*). This assumption carries with it any charge compensation associated with defects' stable configuration (*42, 62*). Depending on their mobilities and efficiencies of various processes, these monomers either mutually recombine or form defect clusters.

4.1 Microstructure evolution model

Current knowledge of defects in ceria is limited to defects that are relevant to SOFC applications, which do not involve cation vacancies and self-interstitials as well as anion self-interstitials (*49, 50, 63, 64*). Thus, to gain further insight into the concentration of cation defects and anion interstitials, we implement a rate theory model (*42, 65, 66*). This is an important step that helps us

gauge the impact of a larger subset of radiation defects on Raman spectroscopy and ellipsometry (*23*).

Our RT model applied to low dose proton irradiation provides a simplified description of the microstructure evolution in this ionic compound by considering three processes, which include monomer generation on cation and anion sublattices, independent recombination of interstitial-vacancy pairs on each sublattice, and defect clustering into stoichiometric dislocation loops (*42*, *65*). Loop nucleation is explicitly considered in the model and is governed by a formation of di-interstitials as the rate limiting species. It neglects intermediate clustering steps and charge states of ions in different defect configurations(*46, 67, 68*). Consideration of more comprehensive modeling that accounts for ion charge and defect clustering is beyond the scope of this work, however this simplified analysis provides a pathway for validation of such a comprehensive model.

Briefly, the rate model is captured by a set of ordinary differential equations of the form (*15*):

$$\frac{\partial C_i}{\partial t} = g - S_{ij} C_i C_j \tag{2}$$

Equation 2 evolves the concentration of each defect type, where indices (*i*,*j*) represent monomers O_I, V_O, Ce_I, and V_{Ce} and loop (L). g is the generation rate defined by the displacement damage for monomers and di-interstitial formation for loop nucleation (*42, 66*). Mutual interaction between defect pair S_{ij} represents recombination for (O_I, V_O) and (Ce_I, V_{Ce}) pairs, di-interstitial formation for two Ce_I acts as loop nucleation. Terms S_{iL} capture absorption of monomers by loops and contribute to loop growth or shrinkage subject to conservation of atoms (*15*)

$$\frac{d}{dt}\left(\frac{\pi b}{3\Omega_0} R_L^2 C_L\right) = S_{iL} C_i C_L, \tag{3}$$

where R_L is loop radius, b is Burger's vector and Ω_0 volume per atom. Each non-zero S_{ij} depends on monomer diffusion coefficient and geometrical factors capturing atomic structure of defects (*65*). S_{ij} were defined in previous publications (*42*) and are reproduced in full form in SI. This model has been parametrized based on the experimental data obtained from TEM, XRD, and thermal conductivity measurements (*27, 42*). The diffusion coefficients are represented using Arrhenius type dependence $D = D_0 e^{-E_m/k_B T}$. Prefactors D_0 for O monomers are chosen based on molecular dynamics simulations for CeO_2 (*69*), while, D_0 for Ce monomers are based on the cation parameters reported for UO_2 (*45, 70*). Migration energy barriers E_m values are reported in Table V. It should be noted that cation interstitial migration is lower than typically obtained from first principles calculations. This effectively lower value has been attributed to an intricate behavior not captured by this simple model where extended defect growth is in fact controlled by the migration of anti-Schottky trios which are found to be more mobile than cation interstitials (*67, 71*).

Table V. Point defect diffusion coefficients used in microstructure evolution modeling.

Defect type	Prefactor, D_0 (cm^2/s) (*45, 69, 70*)	Migration barrier, E_m (eV) (*42*)
Cerium vacancy	0.65	5.0
Cerium interstitial,	0.01	2.66
O vacancy	0.02	0.84
O interstitial	0.01	1.18

Figure 5 shows monomer concentration evolution under two different doses matching the experimental conditions (*14*). Concentrations of both V_{Ce} and Ce_I gradually increase and saturate at values determined by quasi-equilibrium condition, where their production and mutual recombination are equal. Notably, the equilibrium concentration is large for the HF sample.

Concentration of O_I is very small owing to its high mobility and tendency to cluster to dislocation loops unless it recombines with the V_O. Concentration of V_O gradually increases over this dose range. It is orders of magnitude lower than that for V_{Ce} and Ce_I, and this value reflects fraction of V_O defects that have not undergone recombination. Interestingly, V_O concentrations for two cases are comparable and appear to be marginally larger in LF case.

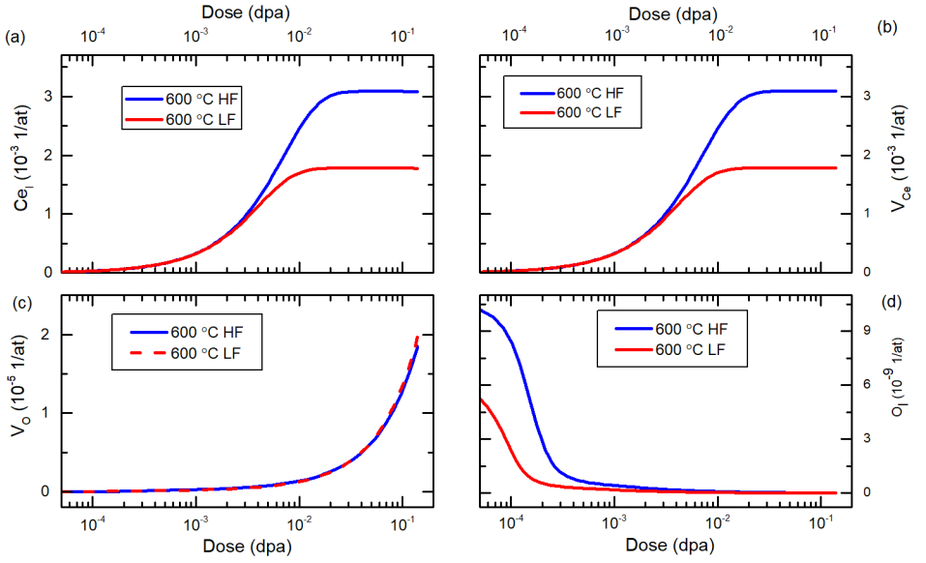

Figure 5. Microstructure evolution in proton irradiated CeO_2 using RT model. Concentration of (a) Ce_I, (b) V_{Ce} (c) V_O, and (d) O_I.

4.2 Vibrational properties

In this section, we discuss the sensitivity of Raman spectra to different defects. First, we discuss the mechanism responsible for each defect peak. Then, we compare their intensities to defect concentration suggested by the RT model. Raman spectra of CeO_2 and similar fluorite structure oxides such as UO_2 and ThO_2 are governed by vibrations within the anion sublattice (*63*). The F_{2g} peak characterized by out-of-phase vibrations of the nearest neighboring oxygen atoms (Fig. 6c)

is triply degenerate and consists of one longitudinal and two transverse optical modes at the Γ-point of the Brillouin zone (*20, 72*). Alternatively, this vibration has been described by the bending of adjacent Ce-O bonds.

The F_{2g} mode peak broadening and shift seen in Fig. 2 (b and c) is consistent with a disorder induced phonon confinement effect (*56, 64*). Under this effect, dispersive optical phonons in the vicinity of the *Γ*-point with non-zero momentum become Raman active and the extent of peak-shift and broadening has been previously correlated to defect concentration (*20*).

The impact of defects on vibrational spectra of doped ceria has been extensively investigated. Particularly, the origin of the two separate peaks at ~560 cm^{-1} and ~590 cm^{-1} has been debated. It has been reported that, in case of an A^{4+} tetravalent ion substitution ($Ce_{1-x}A_xO_2$), a D_2 peak at 590 cm^{-1} emerges, whereas for a B^{3+} trivalent ion substitution ($Ce_{1-x}B_xO_{2-0.5x}$), an additional D_1 peak at 560 cm^{-1} emerges (*20, 56, 64, 73*). The D_1 peak centered at 560 cm^{-1} has been attributed to vibrational modes of an oxygen-vacancy complex represented by an overlapping O_vO_6 octahedron and $O_vCe^{4+}{}_{4-x}A^{3+}{}_x$ tetrahedron complexes (Fig. 6d) (*73, 74*). On the other hand, the D_2 peak has been attributed to the vibration modes of an MO_8 complex associated with cation substitutions (Fig. 6e) (*55, 73-75*). An alternative description for the origin of defect peaks suggests that D_1 and D_2 are attributed to the stretching vibration of Ce^{3+}–O–Ce^{4+} and $M^{3+/4+}$–O–Ce^{4+} bonds (*76*). Assignment of these peaks have been supported by theoretical calculations as well (*63, 77, 78*).

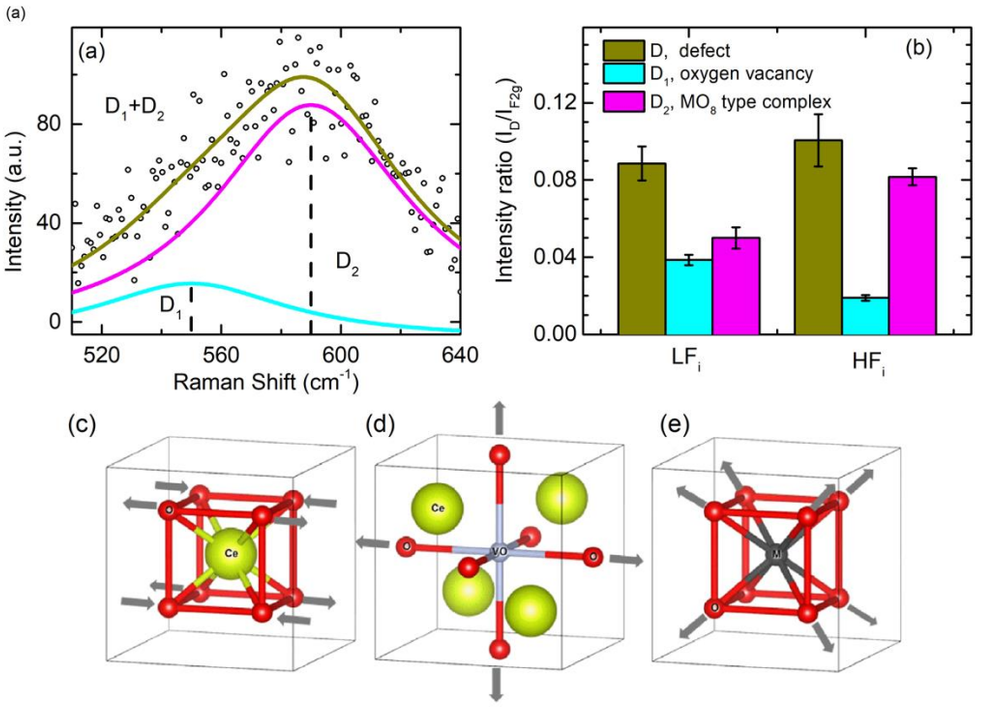

Figure 6. (a) D-peak fitting with the D_1 and D_2 peaks contribution shown separately, (b) ratio of intensities of defect peaks with the F_{2g} peak. (c) F_{2g} vibration mode of perfect CeO_2, (d) atomic complex associated with oxygen vacancy contributing to D_1 peak, (e) MO_8 complex associated with D_2 peak. M represents a cation vacancy of either of atoms in the octahedral interstitial sites. Arrows indicate relative motion of the oxygen atoms in (c) F_{2g} mode, (d) and(e) A_{1g} breathing modes of defect complexes. Note that A_{1g} mode is identified for illustration purpose only and does not necessarily correspond to a motion of atoms associated with D_1 and D_2 peaks.

While these two distinct peaks are not visibly identifiable in our experimental data (Fig. 2a), the previous reports provide sufficient justification to perform the additional peak fitting of the broad D peak in irradiated samples with two isolated Gaussian peaks as shown in Fig. 6(a). The bar plot in Fig. 6(b) summarizes fitting results for D_1 and D_2 peak intensities, whose positions were fixed at 550 and 590 cm^{-1}. We can quantify relative defect density by taking the ratio of the intensity of D, D_1, and D_2 defect peaks to the intensity of the intrinsic F_{2g} peak (*79*). Using a peak assignment consistent with previous reports, the I_{D1} /I_{F2g} ratio shown in Fig. 6(b) suggests that concentration

of oxygen vacancies is larger in the LF sample as compared to the HF. On the other hand, the concentration of defects represented by MO_8 complex is larger in the HF than in the LF sample. Considering absence of dopants and lack of the D_2 peak in the pristine sample, MO_8 complex peak in irradiated samples is likely representing both or either of Ce_I and V_{Ce} defects. The larger magnitude of I_{D2} /I_{F2g} in the HF sample is consistent with RT predictions for Ce_I and V_{Ce} concentrations (Fig. 5). However, the concentration of V_O in irradiated sample is not fully consistent with RT predictions. Instead, modeling suggests that V_O concentrations are comparable under both irradiation conditions. It should be noted that during the model parametrization, it was observed that some sets of diffusion parameters predicted a larger concentration of V_O in the LF sample. However, this behavior remains unexplained. The overall conclusion from Raman analysis is that the likely source of the D_2 peak in the LF and HF samples are cerium sublattice defects, as both have similar MO_8 complex configuration (Fig. 6e).

4.3 Electronic structure of defects

Optical spectroscopy is best suited to study the electronic structure of defects (*21-23*). The narrow 1.4 -3.4 eV range of the ellipsometer used in this work prevented us from complete and optimal characterization of the intrinsic electronic transitions in defect free ceria described by two prominent O2p→Ce4f at 4.1 eV and O2p→Ce5d at 8.3 eV optical transitions (Fig. 7a) (*80*). Nevertheless, the measured dielectric constant spectra of the defect-free sample was found to be consistent with those intrinsic transitions (Fig. 3a).

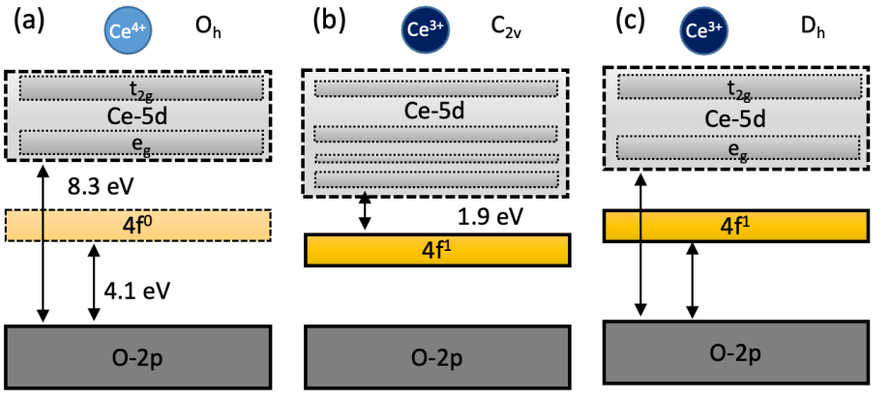

Figure 7. Electronic band diagram of ceria associated with (a) Ce^{4+} ion in O_h environment, (b) Ce^{3+} ions in C_{2v} environment and (c) Ce^{3+} ions in D_{4h} environment.

The observed spectra in irradiated samples allowed us to identify a new defect induced peak located at 1.9 eV (Fig. 4a). This peak has been previously attributed to the formation of Ce^{3+} ions associated with V_O (*81, 82*). Irradiation damage induced defect peaks in ceria thin films has been previously reported by Costantini *et al.*, where the origin of this peak has been attributed to a Ce4f→Ce5d transition that becomes possible in Ce^{3+} ions (Fig. 7b) (*80*). In Ce^{4+}, the 4f orbitals are empty, however when V_O is created by removal of an oxygen atom, two extra electrons remain. Each of these two electrons are localized at the two nearest Ce ions, by becoming Ce^{3+} ions and partially populating 4f orbitals of the respective ions. This localization of electrons is accompanied by additional crystal field splitting of the 5d orbital. The Ce5d bands of Ce^{4+} are already split in two bands of E_g and T_{2g} symmetry owing to octahedral symmetry of perfect CeO_2. The formation of two Ce^{3+} ions next to the V_O changes the local symmetry around the defect to C_{2v} with a strong crystal field effect (*83*). This further splits the 5d-bands apart and pushes one of them closer to the 4f-band making a low energy 4f-5d transition possible (Fig. 7b).

Analysis of the defect peak's oscillator strength provides further support for the assignment of this peak to oxygen vacancies. Intensity of the defect peaks (Table IV) suggest a comparable concentration of Ce^{3+}-V_O type defects in LF and HF samples, which is consistent prediction of RT model.

One aspect that may appear contradictory is the lack of Ce_I in the optical spectra, which, based on previous lattice expansion analysis coupled with the RT model, suggests that it should also contain Ce^{3+} ions (*42*). Presence of Ce^{3+} ions associated with the localization of 4 extra electrons when Ce_I is introduced has been also supported by ab-initio electronic structure calculations (*84*). However, the atomic arrangement of Ce^{3+} ions around Ce_I is likely to have D_{4h} symmetry. A weaker crystal field effect in this environment is not expected to push the 5d band down closer to 4f as in the case of C_{2v} environment, thus explaining lack of 1.9 eV peak associated with Ce_I, despite the presence of Ce^{3+} ions. The weaker crystal field splitting results in a 5d band more similar to pristine Ce^{4+} ceria. The bandgap energy is the difference between 2p→5d and 4f→5d, 4.2 eV. Due to the pristine 2p→5d bandgap in pristine ceria being similar at 4.1 eV, this additional peak would mostly result in a broadened 4.1 eV peak, as opposed to a distinct separate peak.

A summary of defect characterization is depicted in Fig. 8, where we compare the results presented in Figs. 5 and 6 and Tables III and IV in normalized form. All the quantities are normalized to larger value between LF and HF. Fig. 8(a) compares V_{Ce} and Ce_I concentrations from the RT model (Fig. 5) to the magnitude of the F_{2g} peak shift (Table III), as well as the normalized intensity of D_2 peak (Fig. 6), to emphasize similar dependence of the depicted quantities on proton flux. Similar comparison of features related to V_O are shown in Fig. 8(b), which includes prediction of the RT model (Fig. 5) and intensities of the Raman D_1 peak (Fig. 6) and defect peak from ellipsometry (Table IV).

Journal of Applied Physics

AIP Publishing

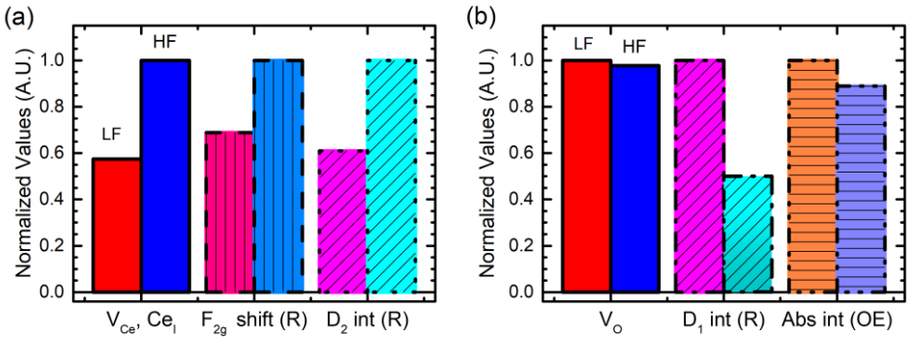

Figure 8. Comparison of optical and Raman spectroscopy and RT model results. Comparison of features that are proportional to (a) cation defect concentrations and (b) oxygen vacancies. Measured values are displayed as textured. Red and blue shades correspond to LF and HF samples, respectively.

5. Conclusions

In conclusion, we applied multiple characterization tools to characterize point defects in proton irradiated CeO_2. A rate model was parametrized based on the dislocation loop characterization using transmission electron microscopy, lattice constant measurement using XRD, and thermal conductivity. Optical ellipsometry exhibits sensitivity primarily to oxygen vacancies accompanied by formation of Ce^{3+}, whereas Raman spectroscopy appears to provide a much broader perspective. While F_{2g} peak broadening and shift provides an integral measure of disorder, the defect peaks have sensitivity to local atomic structure of the defects. At this stage of development, our analysis of the two optical spectroscopies employed is able to reveal qualitative information on defect densities. Further work is needed to establish a correlation that allows defect quantification for optical spectroscopies and Raman peak analysis in ceria and related fluorite oxides.

Supplementary Material

Supplementary material document includes figures for ion beam damage profile and optical index of refraction and a complete set of equations for the RT model.

Acknowledgements

This work was supported by Center for Thermal Energy Transport under Irradiation (TETI), an Energy Frontier Research Center funded by the U.S. Department of Energy, Office of Science, and Office of Basic Energy Sciences.

References:

1. M. Mogensen, N. M. Sammes, G. A. Tompsett, Physical, chemical and electrochemical properties of pure and doped ceria. *Solid State Ionics* **129**, 63-94 (2000).
2. E. C. C. Souza, H. F. Brito, E. N. S. Muccillo, Optical and electrical characterization of samaria-doped ceria. *Journal of Alloys and Compounds* **491**, 460-464 (2010).
3. J.-M. Costantini *et al.*, Defects induced in cerium dioxide single crystals by electron irradiation. *Journal of Applied Physics* **123**, 025901 (2018).
4. H. Sohn *et al.*, Effect of Cobalt on Reduction Characteristics of Ceria under Ethanol Steam Reforming Conditions: AP-XPS and XANES Studies. *Journal of Physical Chemistry C* **120**, 14631-14642 (2016).
5. D. H. Hurley *et al.*, Thermal Energy Transport in Oxide Nuclear Fuel. *Chemical Reviews* **122**, 3711-3762 (2022).
6. R. Thanneeru, S. Patil, S. Deshpande, S. Seal, Effect of trivalent rare earth dopants in nanocrystalline ceria coatings for high-temperature oxidation resistance. *Acta Materialia* **55**, 3457-3466 (2007).
7. I. Kosacki, V. Petrovsky, H. U. Anderson, P. Colomban, Raman spectroscopy of nanocrystalline ceria and zirconia thin films. *Journal of the American Ceramic Society* **85**, 2646-2650 (2002).
8. X. Guo, R. Waser, Electrical properties of the grain boundaries of oxygen ion conductors: Acceptor-doped zirconia and ceria. *Progress in Materials Science* **51**, 151-210 (2006).
9. S. Heiroth *et al.*, Crystallization and grain growth characteristics of yttria-stabilized zirconia thin films grown by pulsed laser deposition. *Solid State Ionics* **191**, 12-23 (2011).
10. S. Beschnitt, T. Zacherle, R. A. De Souza, Computational Study of Cation Diffusion in Ceria. *Journal of Physical Chemistry C* **119**, 27307-27315 (2015).
11. A. Turos, H. Matzke, S. Kwiatkowski, Recovery stages in ${\mathrm{UO}}_{2}$ at low temperatures. *Physical Review Letters* **65**, 1215-1218 (1990).
12. H. Y. Xiao, Y. Zhang, W. J. Weber, Trapping and diffusion of fission products in ThO2 and CeO2. *Journal of Nuclear Materials* **414**, 464-470 (2011).
13. S. J. Zinkle, C. Kinoshita, Defect production in ceramics. *Journal of Nuclear Materials* **251**, 200-217 (1997).
14. M. Khafizov *et al.*, Combining mesoscale thermal transport and x-ray diffraction measurements to characterize early-stage evolution of irradiation-induced defects in ceramics. *Acta Materialia* **193**, 61-70 (2020).
15. C. A. Dennett *et al.*, An integrated experimental and computational investigation of defect and microstructural effects on thermal transport in thorium dioxide. *Acta Materialia*, 116934 (2021).
16. S. I. Golubov, A. V. Barashev, R. E. Stoller, Radiation Damage Theory. *Comprehensive Nuclear Materials, Vol 1: Basic Aspects of Radiation Effects in Solids/Basic Aspects of Multi-Scale Modeling*, 357-391 (2012).
17. G. Balakrishnan *et al.*, X-ray diffraction, Raman and photoluminescence studies of nanocrystalline cerium oxide thin films. *Ceramics International* **39**, 8327-8333 (2013).
18. S. A. Acharya, V. M. Gaikwad, V. Sathe, S. K. Kulkarni, Influence of gadolinium doping on the structure and defects of ceria under fuel cell operating temperature. *Applied Physics Letters* **104**, 113508 (2014).
19. Y. Liu *et al.*, Thermal spike response and irradiation-damage evolution of a defective YAlO3 crystal to electronic excitation. *Journal of Nuclear Materials* **499**, 312-316 (2018).

20. J. T. Graham, Y. W. Zhang, W. J. Weber, Irradiation-induced defect formation and damage accumulation in single crystal CeO2. *Journal of Nuclear Materials* **498**, 400-408 (2018).
21. G. P. Pells, RADIATION-DAMAGE EFFECTS IN ALUMINA. *Journal of the American Ceramic Society* **77**, 368-377 (1994).
22. A. I. Popov, E. A. Kotomin, J. Maier, Basic properties of the F-type centers in halides, oxides and perovskites. *Nuclear Instruments & Methods in Physics Research Section B-Beam Interactions with Materials and Atoms* **268**, 3084-3089 (2010).
23. A. Khanolkar *et al.*, Inferring relative dose-dependent color center populations in proton irradiated thoria single crystals using optical spectroscopy. *Physical Chemistry Chemical Physics* **24**, 6133-6145 (2022).
24. C. Onofri *et al.*, Evolution of extended defects in polycrystalline UO2 under heavy ion irradiation: combined TEM, XRD and Raman study. *Nuclear Instruments & Methods in Physics Research Section B-Beam Interactions with Materials and Atoms* **374**, 51-57 (2016).
25. W.-Y. Chen *et al.*, Characterization of dislocation loops in CeO2 irradiated with high energy Krypton and Xenon. *Philosophical Magazine* **93**, 4569-4581 (2013).
26. C. J. Ulmer, W. Y. Chen, D. E. Wolfe, A. T. Motta, In-situ ion irradiation induced grain growth in nanocrystalline ceria. *Journal of Nuclear Materials* **545**, (2021).
27. M. Khafizov, J. Pakarinen, L. He, D. H. Hurley, Impact of irradiation induced dislocation loops on thermal conductivity in ceramics. *Journal of the American Ceramic Society* **102**, 7533-7542 (2019).
28. F. A. Selim *et al.*, Positron lifetime measurements of hydrogen passivation of cation vacancies in yttrium aluminum oxide garnets. *Physical Review B* **88**, (2013).
29. T. Deng *et al.*, Ti3AlC2, a candidate structural material for innovative nuclear energy system: The microstructure phase transformation and defect evolution induced by energetic heavy-ion irradiation. *Acta Materialia* **189**, 188-203 (2020).
30. R. Mohun *et al.*, Quantification of irradiation-induced defects in UO2 using Raman and positron annihilation spectroscopies. *Acta Materialia* **164**, 512-519 (2019).
31. L. J. Huang *et al.*, Synchrotron radiation x-ray absorption of ion bombardment induced defects on diamond (100). *Journal of Applied Physics* **76**, 7483-7486 (1994).
32. T.-S. Wu *et al.*, Defect engineering by synchrotron radiation X-rays in CeO2 nanocrystals. *Journal of Synchrotron Radiation* **25**, 1395-1399 (2018).
33. C. A. Dennett *et al.*, The influence of lattice defects, recombination, and clustering on thermal transport in single crystal thorium dioxide. *APL Materials* **8**, (2020).
34. V. Chauhan *et al.*, Thermal Conductivity Degradation and Microstructural Damage Characterization in Low-Dose Ion Beam-Irradiated 3C-SiC. *Metallurgical and Materials Transactions E-Materials for Energy Systems* **4**, 61-69 (2017).
35. E. A. Scott *et al.*, Phonon scattering effects from point and extended defects on thermal conductivity studied via ion irradiation of crystals with self-impurities. *Physical Review Materials* **2**, (2018).
36. C. A. Dennett, D. L. Buller, K. Hattar, M. P. Short, Real-time thermomechanical property monitoring during ion beam irradiation using in situ transient grating spectroscopy. *Nuclear Instruments & Methods in Physics Research Section B-Beam Interactions with Materials and Atoms* **440**, 126-138 (2019).
37. Y. Z. Wang *et al.*, Imaging grain microstructure in a model ceramic energy material with optically generated coherent acoustic phonons. *Nature Communications* **11**, (2020).

38. A. Reza, H. B. Yu, K. Mizohata, F. Hofmann, Thermal diffusivity degradation and point defect density in self-ion implanted tungsten. *Acta Materialia* **193**, 270-279 (2020).
39. Y. Z. Wang, G. F. Sha, C. Harlow, M. Yazbeck, M. Khafizov, Impact of nuclear reactor radiation on the performance of AlN/sapphire surface acoustic wave devices. *Nuclear Instruments & Methods in Physics Research Section B-Beam Interactions with Materials and Atoms* **481**, 35-41 (2020).
40. J. Rest, G. L. Hofman, An alternative explanation for evidence that xenon depletion, pore formation, and grain subdivision begin at different local burnups. *Journal of Nuclear Materials* **277**, 231-238 (2000).
41. L. F. He *et al.*, Bubble formation and Kr distribution in Kr-irradiated UO2. *Journal of Nuclear Materials* **456**, 125-132 (2015).
42. V. S. Chauhan *et al.*, Indirect characterization of point defects in proton irradiated ceria. *Materialia* **15**, 101019 (2021).
43. C. Kinoshita, K. Hayashi, S. Kitajima, Kinetics of Point-defects in electron-irradiated MgO. *Nuclear Instruments & Methods in Physics Research Section B-Beam Interactions with Materials and Atoms* **1**, 209-218 (1984).
44. J. P. Crocombette, Influence of charge states on energies of point defects and clusters in uranium dioxide. *Physical Review B* **85**, (2012).
45. S. Khalil, T. Allen, A. El-Azab, Off-stoichiometric defect clustering in irradiated oxides. *Chemical Physics* **487**, 1-10 (2017).
46. C. Matthews, R. Perriot, M. W. D. Cooper, C. R. Stanek, D. A. Andersson, Cluster dynamics simulation of uranium self-diffusion during irradiation in UO2. *Journal of Nuclear Materials* **527**, (2019).
47. J. F. Ziegler, M. D. Ziegler, J. P. Biersack, SRIM – The stopping and range of ions in matter (2010). *Nuclear Instruments and Methods in Physics Research Section B: Beam Interactions with Materials and Atoms* **268**, 1818-1823 (2010).
48. S. Guo, H. Arwin, S. N. Jacobsen, K. Järrendahl, U. Helmersson, A spectroscopic ellipsometry study of cerium dioxide thin films grown on sapphire by rf magnetron sputtering. *Journal of Applied Physics* **77**, 5369-5376 (1995).
49. F. Marabelli, P. Wachter, Covalent insulator ${\mathrm{CeO}}_{2}$: Optical reflectivity measurements. *Physical Review B* **36**, 1238-1243 (1987).
50. P. Patsalas, S. Logothetidis, C. Metaxa, Optical performance of nanocrystalline transparent ceria films. *Applied Physics Letters* **81**, 466-468 (2002).
51. N. Ishikawa *et al.*, Study of structural change in CeO2 irradiated with high-energy ions by means of X-ray diffraction measurement. *Nuclear Instruments and Methods in Physics Research Section B: Beam Interactions with Materials and Atoms* **266**, 3033-3036 (2008).
52. D. Manara, B. Renker, Raman spectra of stoichiometric and hyperstoichiometric uranium dioxide. *Journal of Nuclear Materials* **321**, 233-237 (2003).
53. K. Rickert *et al.*, Assessing UO2 sample quality with mu-Raman spectroscopy. *Journal of Nuclear Materials* **514**, 1-11 (2019).
54. T. Livneh, E. Sterer, Effect of pressure on the resonant multiphonon Raman scattering in UO2. *Physical Review B* **73**, 085118 (2006).
55. T. Taniguchi *et al.*, Identifying Defects in Ceria-Based Nanocrystals by UV Resonance Raman Spectroscopy. *The Journal of Physical Chemistry C* **113**, 19789-19793 (2009).

56. W. H. Weber, K. C. Hass, J. R. McBride, Raman study of ${\mathrm{CeO}}_{2}$: Second-order scattering, lattice dynamics, and particle-size effects. *Physical Review B* **48**, 178-185 (1993).
57. H. He, D. Shoesmith, Raman spectroscopic studies of defect structures and phase transition in hyper-stoichiometric UO2+x. *Physical Chemistry Chemical Physics* **12**, 8109-8118 (2010).
58. G. Guimbretière *et al.*, Determination of in-depth damaged profile by Raman line scan in a pre-cut He2+ irradiated UO2. *Applied Physics Letters* **100**, 251914 (2012).
59. G. E. Jellison, F. A. Modine, Parameterization of the optical functions of amorphous materials in the interband region. *Applied Physics Letters* **69**, 371-373 (1996).
60. M. Balestrieri *et al.*, - Photoluminescence properties of rare earth (Nd, Yb, Sm, Pr)-doped CeO2 pellets prepared by solid-state reaction. - *Journal of Materials Chemistry C*, - 7014.
61. H. Matzke, O. Meyer, A. Turos, Damage recovery in the U-sublattice of ion implanted UO2 between 5 K and 2000 K. *Radiation Effects and Defects in Solids* **119-121**, 885-890 (1991).
62. S. Grieshammer, T. Zacherle, M. Martin, Entropies of defect formation in ceria from first principles. *Physical Chemistry Chemical Physics* **15**, 15935-15942 (2013).
63. A. Nakajima, A. Yoshihara, M. Ishigame, Defect-induced Raman-spectra in doped CeO2. *Physical Review B* **50**, 13297-13307 (1994).
64. J. R. McBride, K. C. Hass, B. D. Poindexter, W. H. Weber, Raman and x-ray studies of Ce1−xRExO2−y, where RE=La, Pr, Nd, Eu, Gd, and Tb. *Journal of Applied Physics* **76**, 2435-2441 (1994).
65. L. He *et al.*, Phase and defect evolution in Uranium-Nitrogen-Oxygen system under irradiation. *Acta Materialia*, 116778 (2021).
66. L. He *et al.*, Dislocation Loop Evolution in Kr-Irradiated ThO_2. *J. Amer. Ceram. Soc.*, (2022).
67. C. Jiang *et al.*, Unraveling small-scale defects in irradiated ThO2 using kinetic Monte Carlo simulations. *Scripta Materialia* **214**, 114684 (2022).
68. S. Kumar Mazumder, M. Kaur Salaken Singh, T. Kumagai, A. El-Azab, Atomistically-informed modeling of point defect clustering and evolution in irradiated ThO2. *Chemical Physics*, 111645 (2022).
69. S. P. Waldow, R. A. De Souza, Is excess faster than deficient? A molecular-dynamics study of oxygen-interstitial and oxygen-vacancy diffusion in CeO2. *Journal of Physics: Energy* **2**, 024001 (2020).
70. D. A. Andersson *et al.*, Multiscale simulation of xenon diffusion and grain boundary segregation in UO2. *Journal of Nuclear Materials* **462**, 15-25 (2015).
71. X. Y. Liu, D. A. Andersson, Small uranium and oxygen interstitial clusters in UO2: An empirical potential study. *Journal of Nuclear Materials* **547**, (2021).
72. V. G. Keramidas, W. B. White, Raman spectra of oxides with the fluorite structure. *The Journal of Chemical Physics* **59**, 1561-1562 (1973).
73. L. Li, F. Chen, J.-Q. Lu, M.-F. Luo, Study of Defect Sites in Ce1–xMxO2−δ (x = 0.2) Solid Solutions Using Raman Spectroscopy. *The Journal of Physical Chemistry A* **115**, 7972-7977 (2011).
74. P. Sudarsanam, K. Kuntaiah, B. M. Reddy, Promising ceria–samaria-based nano-oxides for low temperature soot oxidation: a combined study of structure–activity properties. *New Journal of Chemistry* **38**, 5991-6001 (2014).

75. T. Taniguchi *et al.*, Identifying Defects in Ceria-Based Nanocrystals by UV Resonance Raman Spectroscopy. *Journal of Physical Chemistry C* **113**, 19789-19793 (2009).
76. Y. X. Xu *et al.*, Resolving a Decade-Long Question of Oxygen Defects in Raman Spectra of Ceria-Based Catalysts at Atomic Level. *Journal of Physical Chemistry C* **123**, 18889-18894 (2019).
77. C. Schilling, A. Hofmann, C. Hess, M. V. Ganduglia-Pirovano, Raman Spectra of Polycrystalline CeO2: A Density Functional Theory Study. *Journal of Physical Chemistry C* **121**, 20834-20849 (2017).
78. T. M. Haridasan, J. Govindarajan, M. A. Nerenberg, P. W. M. Jacobs, Impurity modes due to interstitials in CaF2. *Physical Review B* **20**, 3462-3473 (1979).
79. K. Kuntaiah, P. Sudarsanam, B. M. Reddy, A. Vinu, Nanocrystalline Ce1-xSmxO2-delta (x=0.4) solid solutions: structural characterization versus CO oxidation. *Rsc Advances* **3**, 7953-7962 (2013).
80. J.-M. Costantini *et al.*, Optical reflectivity of ion-irradiated cerium dioxide sinters. *Journal of Applied Physics* **126**, 175902 (2019).
81. P. Dorenbos, $5d$-level energies of ${\mathrm{Ce}}^{3+}$ and the crystalline environment. I. Fluoride compounds. *Physical Review B* **62**, 15640-15649 (2000).
82. P. Dorenbos, Charge transfer bands in optical materials and related defect level location. *Optical Materials* **69**, 8-22 (2017).
83. S. K. Hoffmann, J. Goslar, Crystal field theory and EPR parameters in D2d and C2v distorted tetrahedral copper(II) complexes. *Journal of Solid State Chemistry* **44**, 343-353 (1982).
84. P. R. L. Keating, D. O. Scanlon, B. J. Morgan, N. M. Galea, G. W. Watson, Analysis of Intrinsic Defects in CeO2 Using a Koopmans-Like GGA plus U Approach. *Journal of Physical Chemistry C* **116**, 2443-2452 (2012).

Journal of Applied Physics

AIP Publishing

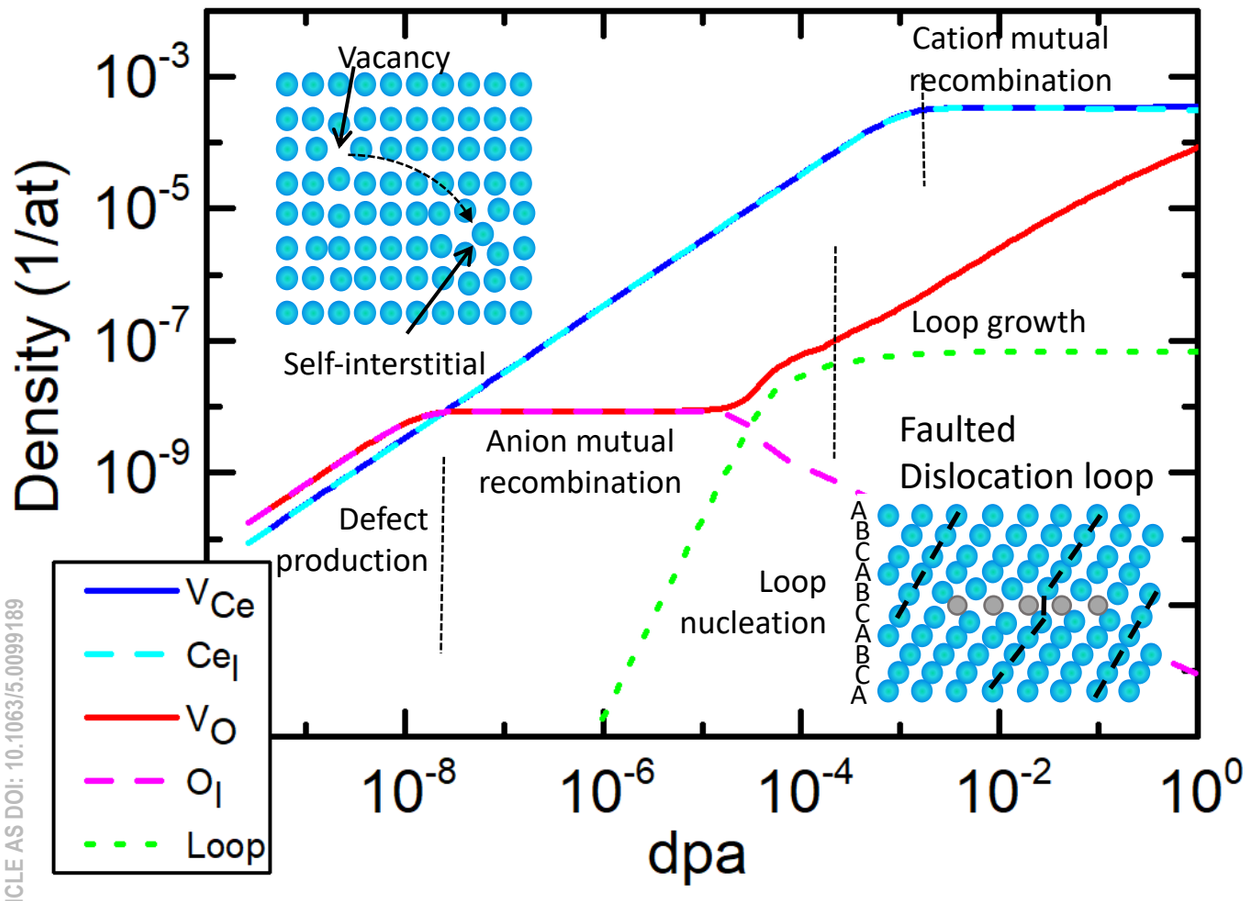

Microscopic lattice expansion

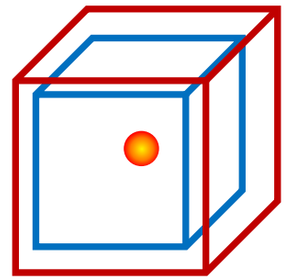

Defect relaxation volume

Defect vibrational properties

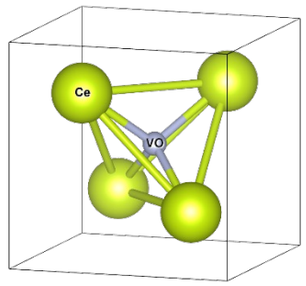

$MO_4 – V_O$

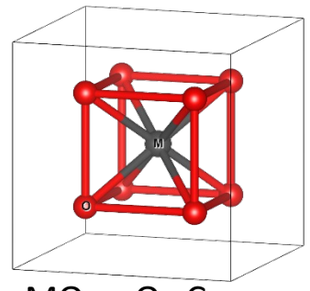

$MO_8 – O_i$, Ce_i,, and V_{Ce}

Defect electronic structure

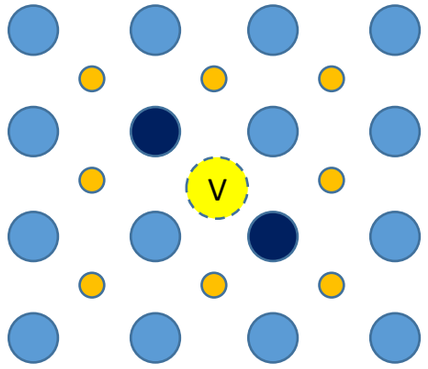

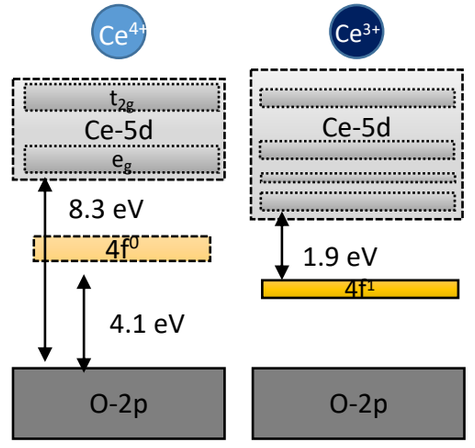

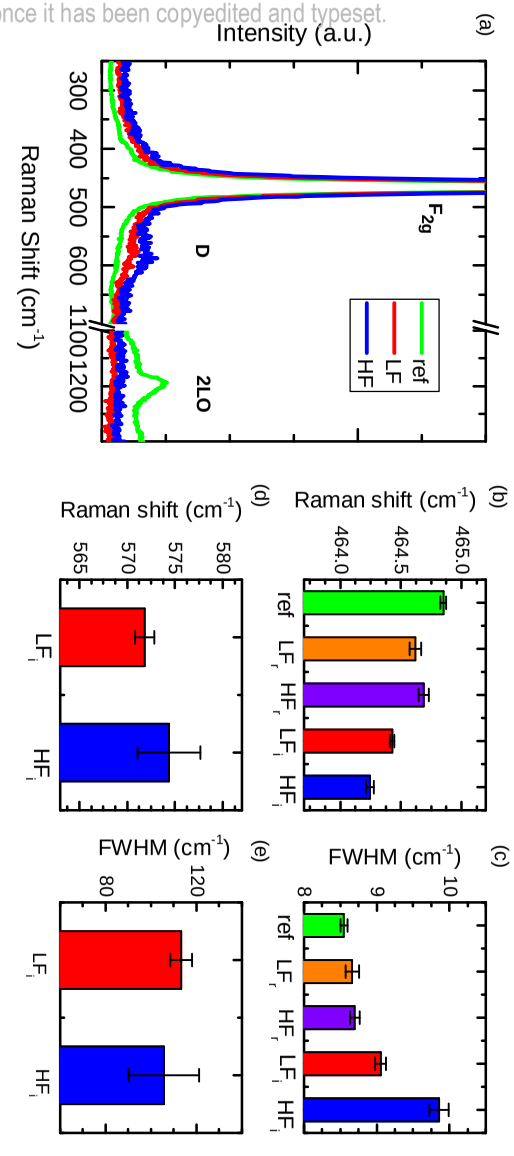

AIP Publishing

Journal of Applied Physics

ACCEPTED MANUSCRIPT

This is the author's peer reviewed, accepted manuscript. However, the online version of record will be different from this version once it has been copyedited and typeset.
PLEASE CITE THIS ARTICLE AS DOI: 10.1063/5.0099189

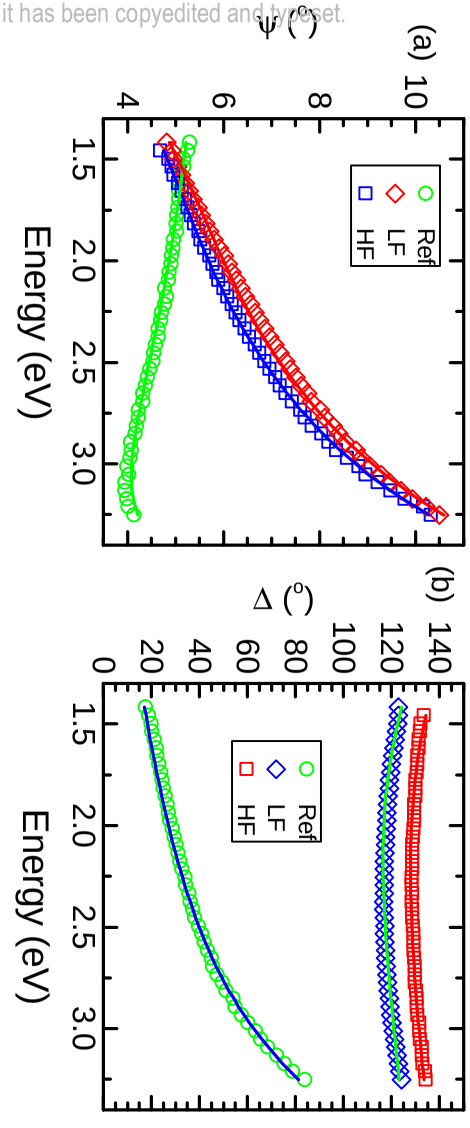

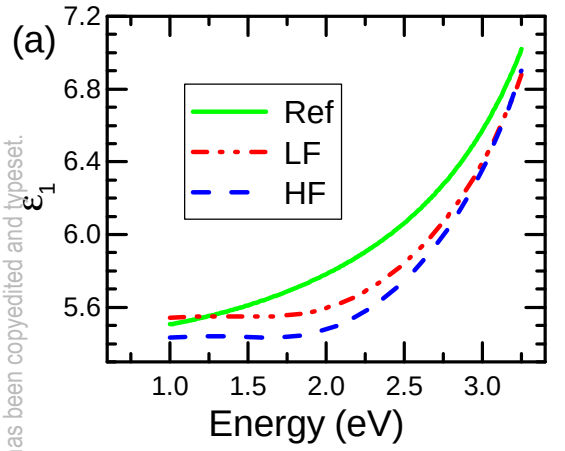

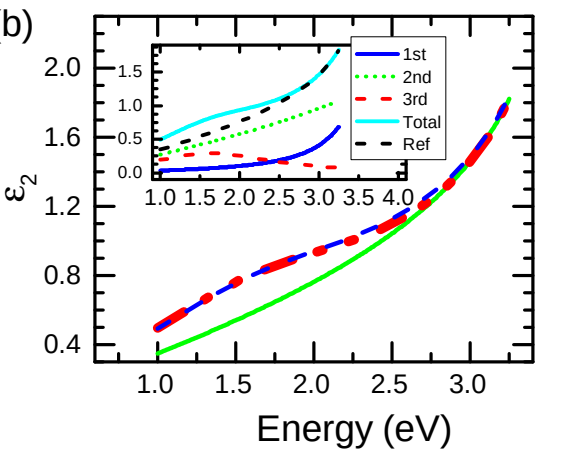

Journal of Applied Physics
AIP Publishing

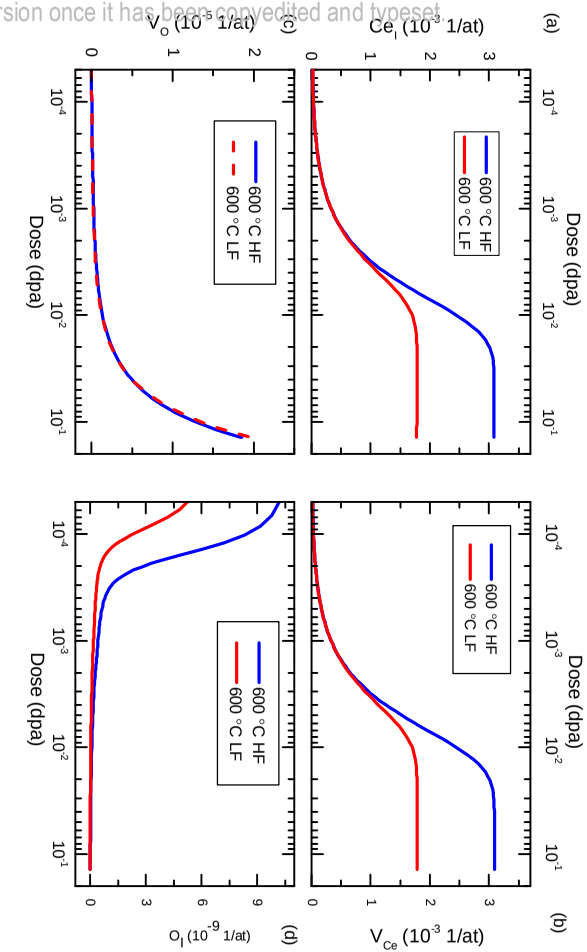

AIP Publishing

Journal of Applied Physics

ACCEPTED MANUSCRIPT

PLEASE CITE THIS ARTICLE AS DOI: 10.1063/5.0099189

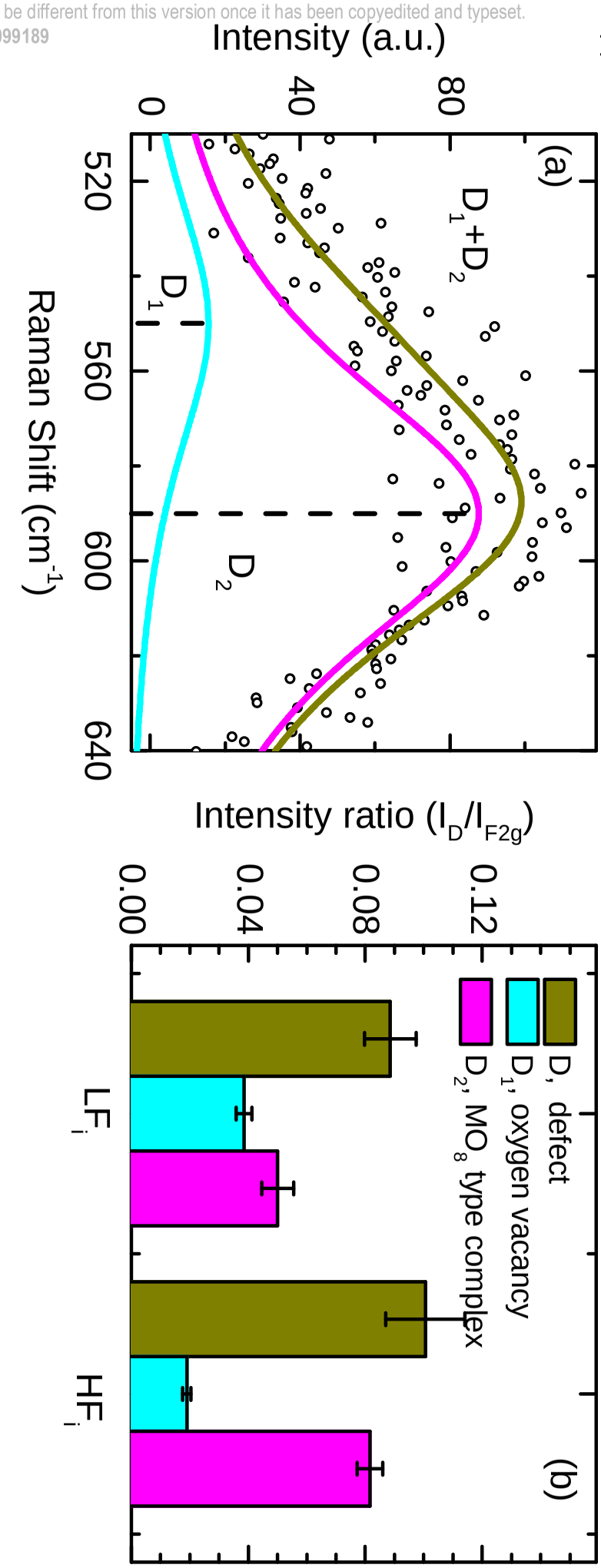

Journal of Applied Physics

ACCEPTED MANUSCRIPT

This is the author's peer reviewed, accepted manuscript. However, the online version of record will be different from this version once it has been copyedited and typeset.
PLEASE CITE THIS ARTICLE AS DOI: 10.1063/5.0099189

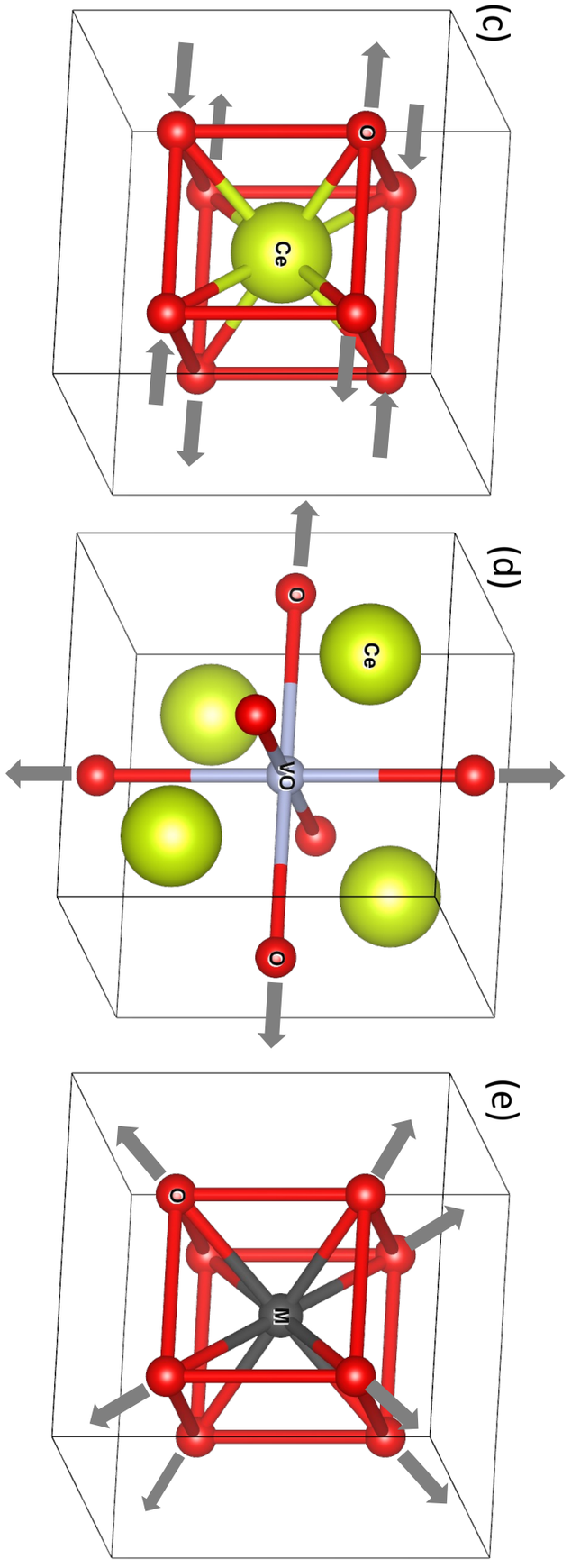

AIP Publishing

Journal of Applied Physics

ACCEPTED MANUSCRIPT

This is the author's peer reviewed, accepted manuscript. However, the online version of record will be different from this version once it has been copyedited and typeset.
PLEASE CITE THIS ARTICLE AS DOI: 10.1063/5.0099189